International Journal of Applied Earth Observations and Geoinformation 97 (2021) 102288

Contents lists available at ScienceDirect

International Journal of Applied Earth Observations and Geoinformation

journal homepage: www.elsevier.com/locate/jag

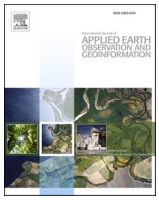

Satellite-derived global chlorophyll-*a* anomaly products

Menghua Wang [a,*], Lide Jiang [a,b], Karlis Mikelsons [a,c], Xiaoming Liu [a,b]

[a] NOAA National Environmental Satellite, Data, and Information Service, Center for Satellite Applications and Research, E/RA3, 5830 University Research Ct., College Park, MD 20740, USA
[b] CIRA at Colorado State University, Fort Collins, CO, USA
[c] Global Science and Technology, 7855 Walker Drive, Suite 200, Maryland, USA

ARTICLE INFO

Keywords:
Chlorophyll-*a*
Chlorophyll-*a* anomaly
Algae blooms
Remote sensing
VIIRS

ABSTRACT

We describe our effort to produce the first-ever near-real-time (NRT) global daily chlorophyll-*a* (Chl-*a*) anomaly products that can be used to detect and identify algae blooms from satellite ocean color measurements such as those from the Visible Infrared Imaging Radiometer Suite (VIIRS) onboard the Suomi National Polar-orbiting Partnership (SNPP) and NOAA-20. Specifically, the production of the two Chl-*a* anomaly products, one for the Chl-*a* anomaly in difference and another for the Chl-*a* anomaly ratio (or in its relative difference) compared to the 61-day Chl-*a* median value from the previous time period (as a Chl-*a* reference), has been implemented in the daily global NRT satellite data processing. These two Chl-*a* anomaly products represent the global ocean and coastal/inland water Chl-*a* abnormal condition for a given location and can provide more complete characteristics for the daily phytoplankton (or algae) biomass status by comparing to the normal condition. Detailed satellite Chl-*a* anomaly algorithms, the implementation of the algorithms in the routine satellite data processing, and the global data processing procedure are described and discussed. In addition, we provide several specific examples from the VIIRS-measured global daily Chl-*a* anomaly products to demonstrate various applications in the detection of algae blooms, including the harmful algal blooms (HABs), in various ocean and coastal/inland waters. Some quantitative seasonal and interannual evaluations and characterizations of Chl-*a* anomalies over global oceans and several coastal/inland waters are also provided and discussed.

1. Introduction

Chlorophyll-*a* (Chl-*a*) concentration over global ocean and coastal/inland waters is one of the most important parameters needed to measure water optical, biological, and biogeochemical properties and their impact on environmental and ecological variations, as well as their influence on global climatic change. In fact, the main objective of the initial satellite ocean color missions, such as the Coastal Zone Color Scanner (CZCS) as a proof-of-concept mission (Gordon et al., 1980; Hovis et al., 1980), is to provide global ocean phytoplankton Chl-*a* (or biomass) concentration distribution and its temporal/spatial variations. Indeed, accurate measurements of the Chl-*a* variation, e.g., long-term Chl-*a* trends over global ocean or short-term Chl-*a* variations over coastal and inland waters, are critical to fully understand the impact of environmental variations on climate change. In fact, the short-term Chl-*a* variations can also represent and quantify the abnormal algae biomass condition in the regional environmental status, in particular, for detecting harmful algal blooms (HABs) in coastal and inland waters, which have significantly impacted the regional and local water conditions as well as people's daily life (IOCCG, 2018; Stumpf et al., 2003).

Since the success of the CZCS mission, there have been continuous satellite ocean color missions for providing global Chl-*a* distribution with high spatial and temporal coverage, including the Sea-viewing Wide-field-of-view Sensor (SeaWiFS) (McClain et al., 2004), the Moderate Resolution Imaging Spectroradiometer (MODIS) on the Terra and Aqua satellites (Esaias et al., 1998; Salomonson et al., 1989), the Medium-Resolution Imaging Spectrometer (MERIS) on the Envisat (Rast et al., 1999), the Visible Infrared Imaging Radiometer Suite (VIIRS) on the Suomi National Polar-orbiting Partnership (SNPP) and NOAA-20 (Goldberg et al., 2013), the Ocean and Land Color Instrument (OLCI) on the Sentinel-3A and Sentinel-3B (Donlon et al., 2012), and the Second-Generation Global Imager (SGLI) on the Global Change Observation Mission-Climate (GCOM-C) (Tanaka et al., 2009). In the last several decades, satellite ocean color data (particularly routine global daily Chl-*a* distribution data) have been widely used for scientific research and various applications (IOCCG, 2008, 2018; McClain, 2009). Certainly, satellite ocean/water color remote sensing will continue in

* Corresponding author.

https://doi.org/10.1016/j.jag.2020.102288
Received 8 October 2020; Received in revised form 12 December 2020; Accepted 16 December 2020
Available online 13 January 2021

order to meet increased demanding for the monitoring of global ocean, coastal, and inland water properties and their variations (Groom et al., 2019; IOCCG, 2012, 2018).

Providing routine accurate global Chl-*a* distribution is obviously quite important and useful in understanding global ocean/water optical, biological, and biogeochemical properties. On the other hand, Chl-*a* (phytoplankton biomass) variation (or its change) compared with its normal condition can provide other crucial water property information. In fact, it is often more useful to understand and monitor Chl-*a* variations for various real applications, which impact our daily life significantly, e.g., HABs (Stumpf, 2001; Stumpf et al., 2003; Tomlinson et al., 2004), and various other types of algae blooms in global coastal and inland waters (Hu et al., 2010; IOCCG, 2018; Shi and Wang, 2009a; Wang et al., 2011). There are various approaches in remote sensing to detect algae blooms (and/or surface floating algae blooms), including the maximum chlorophyll index (MCI) method (Gower et al., 2005; Gower et al., 2008), the floating algae index (FAI) approach (Hu, 2009), the normalized difference algae index (NDAI) method (Shi and Wang, 2009a), and simply using routine global false color imagery (Qi et al., 2020). On the other hand, there has been a significant effort to routinely monitor and detect the regional HABs (as an operational product), e.g., over the Gulf of Mexico (GOM) and Florida coastal regions using the Chl-*a* anomaly product (i.e., Chl-*a* anomaly in difference for detecting Chl-*a* abnormal values) (Stumpf, 2001; Stumpf et al., 2003; Tomlinson et al., 2004). The Chl-*a* anomaly product can typically be used to reliably detect and monitor abnormal Chl-*a* cases with high algae biomass events over global ocean, coastal and inland waters. Therefore, it is useful to have a system for routine production of daily Chl-*a* anomaly products for easy evaluation and monitoring of algae biomass variations over the global open ocean and coastal/inland waters.

In this study, we present our work and effort for routinely producing global daily near-real-time (NRT) Chl-*a* anomaly products using VIIRS measurements. We first describe VIIRS-measured high quality global ocean color product suite (including Chl-*a*), which has been routinely produced. Next, two Chl-*a* anomaly products are defined. Specifically, one is the Chl-*a* anomaly in difference which has been used for detecting the HABs in the GOM and Florida coastal regions (Stumpf, 2001; Stumpf et al., 2003; Tomlinson et al., 2004). In addition, we define and develop an additional Chl-*a* anomaly product with emphasis in its Chl-*a* anomaly in relative difference (Chl-*a* anomaly ratio). We show that using both Chl-*a* anomaly products, one in difference and another in relative difference, can provide more complete information of the ocean/water biomass status, which includes Chl-*a* changes in its spatial and temporal variations. The two Chl-*a* anomaly products represent Chl-*a* changes compared to a normal Chl-*a* condition for the region, not only in the difference of Chl-*a* values, but also with its relative difference of Chl-*a* value changed. Using routine daily global NRT Chl-*a* anomaly products, we can easily identify regions with significant biomass changes compared to the normal condition and further focus on these regions to do more detailed studies with other tools and data, e.g., high spatial and/or hyperspectral measurements from other satellites for more details in the spatial coverage and algae species, e.g., an approach demonstrated in Qi et al. (2020).

2. Global Chl-*a* anomaly products

2.1. VIIRS ocean color products

Since its successful launch in October 2011, VIIRS-SNPP has been routinely providing global land, atmosphere, cryosphere, and ocean data products (Goldberg et al., 2013). In fact, one of the main objectives of the VIIRS satellite series is to provide the research and user communities with continuity of Earth remote sensing data from those of MODIS, which started in 1999 on the Terra and 2002 on the Aqua satellites (Esaias et al., 1998; Salomonson et al., 1989). In particular, the Joint Polar Satellite System (JPSS) program, which started the environmental observing satellite series with the NOAA-20 satellite launched in November 2017, is to provide operational satellite Earth remote sensing products for U.S. and international users for various research and applications. In fact, the VIIRS series will provide several decades long satellite Earth observations for scientific research and user communities globally (Goldberg et al., 2013).

VIIRS spectral characteristics are similar to those of MODIS with a total of 22 spectral bands covering the spectral wavelengths from 0.41 to 12.01 μm. In particular, for global ocean color and coastal/inland water applications, VIIRS-SNPP seven moderate-resolution bands (M-bands, 750 m) M1–M7 for the visible and near-infrared (NIR) at the nominal center wavelengths of 410, 443, 486, 551, 671, 745, and 862 nm, two high-spatial resolution (375 m) imagery bands (I-bands) I1 and I2 at the wavelengths of 638 and 862 nm, and the three shortwave infrared (SWIR) M-bands at the wavelengths of 1238, 1601, and 2257 nm are used for deriving global ocean color products (Wang and Jiang, 2018; Wang et al., 2013). The standard VIIRS ocean color product suite includes the normalized water-leaving radiance $nL_w(\lambda)$ spectra at the VIIRS spectral bands (Wang and Jiang, 2018; Wang et al., 2013), Chl-*a* concentration (Hu et al., 2012; O'Reilly et al., 1998; O'Reilly and Werdell, 2019; Wang and Son, 2016), the water diffuse attenuation coefficient at the wavelength of 490 nm $K_d(490)$ (Lee et al., 2005; Wang et al., 2009) and at the domain of the photosynthetically available radiation (PAR) K_d(PAR) (Morel et al., 2007; Son and Wang, 2015), as well as a quality assurance (QA) product (Wei et al., 2016). In addition, there are several experimental products, e.g., ocean/water inherent optical properties (IOPs) (Lee et al., 2002; Shi and Wang, 2019a; Werdell et al., 2013). Some research products using VIIRS measurements have also been demonstrated, e.g., concentration of suspended particular matter (SPM) (or total suspended matter (TSM)) (Shi et al., 2018; Yu et al., 2019), suspended particle size distribution in global turbid waters (Shi and Wang, 2019b), and shallow water bathymetry data (Wei et al., 2020). Furthermore, in order to meet users' requirements, some new ocean color products have been developed, e.g., routine daily global NRT VIIRS SNPP and NOAA-20 merged and gap-free Chl-*a* data (Liu and Wang, 2018, 2019a, b), routine daily global NRT false-colored red–greenblue (FRGB) imagery for surface floating algae detection using the NOAA online Ocean Color Viewer (OCView) (Mikelsons and Wang, 2018; Qi et al., 2020), as well as super-resolved high spatial resolution VIIRS ocean color products using the deep convolutional neural network (CNN) technique (Liu and Wang, 2021).

VIIRS ocean color products have been derived using the Multi-Sensor Level-1 to Level-2 (MSL12) ocean color data processing system with both the NIR- and SWIR-based atmospheric correction algorithms (Gordon and Wang, 1994; Jiang and Wang, 2014; Wang, 2007; Wang and Shi, 2005, 2007) for the open ocean and turbid coastal/inland waters. MSL12 has been used as the NOAA official ocean color data processing system for VIIRS and other satellite ocean color sensors (Wang et al., 2013), and in fact this data processing software package was developed in the late 1990s for generating consistent ocean color products from various satellite ocean color sensors using a common data processing system (Wang, 1999; Wang and Franz, 2000; Wang et al., 2002).

Significant efforts are being made to evaluate and validate VIIRS-derived ocean color products by the NOAA Ocean Color Team and VIIRS Ocean Color calibration and validation (Cal/Val) team, including annual dedicated Cal/Val cruises from 2014 to collect in situ data, with the most recent one completed in September 2019. Indeed, the NOAA VIIRS ocean color Cal/Val team has successfully carried out five dedicated Cal/Val cruises since 2014. Detailed in situ data measurements and specific procedures in the Cal/Val cruises have been documented and published, e.g., see the two recent 2016 and 2018 cruise reports (Ondrusek et al., 2017; Ondrusek et al., 2019). In addition, through various presentations in conferences and meetings, as well as publications in peer-reviewed journals, good data quality of the VIIRS-derived ocean color products has been well demonstrated and documented

Table 1
Information of the corresponding 24 Chl-$a^{(Clim)}$ reference data for ΔChl-a and ΔrChl-a computations. Note that for the leap year, the periods are listed only for those different from the normal year.

Information for the 24 Chl-$a^{(Clim)}$ Data			
Number	Coverage Time Period	Dates Used for Chl-$a^{(Clim)}$ Computation (date in mm/dd)	
		Normal Year	Leap Year
1, 2	January 1–14, 15–31	10/18–12/17, 11/01–12/31	
3, 4	February 1–14, 15–28[†]	11/18–01/17, 12/02–01/31	
5, 6	March 1–14, 15–31	12/16–02/14, 12/30–02/28	12/17–02/15, 12/31–02/29
7, 8	April 1–14, 15–30	01/16–03/17, 01/30–03/31	01/17–03/17, 01/31–03/31
9, 10	May 1–14, 15–31	02/15–04/16, 03/01–04/30	02/16–04/16,
11, 12	June 1–14, 15–30	03/18–05/17, 04/01–05/31	
13, 14	July 1–14, 15–31	04/17–06/16, 05/01–06/30	
15, 16	August 1–14, 15–31	05/18–07/17, 06/01–07/31	
17, 18	September 1–14, 15–30	06/18–08/17, 07/02–08/31	
19, 20	October 1–14, 15–31	07/18–09/16, 08/01–09/30	
21, 22	November 1–14, 15–30	08/18–10/17, 09/01–10/31	
23, 24	December 1–14, 15–31	09/17–11/16, 10/01–11/30	

[†] Leap year period is February 15–29.

over open oceans and coastal/inland waters (Barnes et al., 2019; Hlaing et al., 2013; Hu et al., 2020; Mikelsons et al., 2020; Shi et al., 2020; Son and Wang, 2020; Wang et al., 2016; Wang et al., 2020). In particular, compared with the in situ Chl-a measurements, Chl-a data over global open oceans are within accuracy of ~30% (usually much better), providing a good basis for deriving other Chl-a-related products, e.g., Chl-a anomaly products, which are described in detail in the next section.

2.2. Chl-a anomaly products

Using VIIRS-measured daily Chl-a data, global daily Chl-a anomaly products can be calculated based on the estimated 61-day climatology Chl-a (as a Chl-a reference) and VIIRS-measured Chl-a on a specific day. The specific procedure and calculation for deriving Chl-a anomaly products are described below.

2.2.1. Calculation of the 61-day Chl-a climatology Chl-$a^{(Clim)}$

The 61-day Chl-a climatology data, Chl-$a^{(Clim)}$, are calculated as Chl-a references based on experiences from a NOAA HAB detection project in the South Florida coast and GOM regions (Stumpf, 2001; Stumpf et al., 2003; Tomlinson et al., 2004). Specifically, the 61-day Chl-a climatology (Chl-$a^{(Clim)}$) data are computed as median values of satellite-derived Chl-a data from the 61-day period, and then calculated on the first day and fifteenth day of each month. Therefore, for each year there are actually 24 data sets of the 61-day Chl-$a^{(Clim)}$ data. The main reason for computing the Chl-a climatology in a 61-day period is because a two-month period is long enough to provide a valid seasonal average Chl-a value, while it is also reasonably short enough to represent the current Chl-a seasonal features (Stumpf et al., 2003; Tomlinson et al., 2004). In addition, the 61-day Chl-$a^{(Clim)}$ data are calculated with a 15-day lag time to avoid anomalous Chl-a values that would significantly impact the Chl-a anomaly calculations for the period. Obviously, it is important to build a reliable Chl-$a^{(Clim)}$ to be used as a reference for Chl-a anomaly estimation, assuming that Chl-$a^{(Clim)}$ data are representative of the normal Chl-a values in the region for the period.

Therefore, based on the above described procedure, for example, Chl-$a^{(Clim)}$ data for June 1 is computed from the median Chl-a values of the 61-day Chl-a data derived from the time period of March 18 to May 17, while for June 15 the 61-day Chl-$a^{(Clim)}$ data are from the time period of April 1 to May 31. Specifically, the June 1 Chl-$a^{(Clim)}$ data are used for Chl-a anomaly estimation for the time period of June 1–14, while the June 15 Chl-$a^{(Clim)}$ data are used for the Chl-a anomaly data covering the time period of June 15–30. It is particularly noted that, during the period of June 1–14 (or June 15–30), Chl-$a^{(Clim)}$ data are the same, i.e., using the June 1 (or June 15) Chl-$a^{(Clim)}$ data. For the months with 31 days or less than 30 days, Chl-$a^{(Clim)}$ data computed on the 15th day cover the time period of day 15 to the end of the month. Table 1 provides the information for the corresponding 24 Chl-$a^{(Clim)}$ reference data, specifically indicating the coverage time period and the time period for Chl-a data used for the calculation of the corresponding Chl-$a^{(Clim)}$. In Table 1, some differences for the leap years, i.e., one coverage time period and five time periods for computing Chl-$a^{(Clim)}$ data, are also listed. All other time periods for the corresponding Chl-$a^{(Clim)}$ data are the same between normal and leap years.

2.2.2. Calculation of the Chl-a anomaly ΔChl-a

With the computed 61-day Chl-$a^{(Clim)}$ data, Chl-a anomaly ΔChl-a for a specific day can be calculated. The Chl-a anomaly ΔChl-a is computed as Chl-a difference between VIIRS-measured Chl-a on that day and the 61-day Chl-$a^{(Clim)}$ data, i.e.,

$$\Delta Chl\text{-}a = Chl\text{-}a - Chl\text{-}a^{(Clim)}, \quad (1)$$

where Chl-$a^{(Clim)}$ is the 61-day Chl-a climatology data (as Chl-a references). As discussed previously, for each month there are two Chl-$a^{(Clim)}$ references for covering time periods of days 1–14 and days 15 to the end of the month.

2.2.3. Calculation of the Chl-a anomaly ratio ΔrChl-a

Using the computed Chl-$a^{(Clim)}$ data, Chl-a anomaly ratio (or Chl-a anomaly in relative difference) ΔrChl-a for a specific day can be defined and calculated. The Chl-a anomaly ratio (or relative difference) ΔrChl-a is calculated as the ratio between the Chl-a anomaly ΔChl-a on that day and the 61-day Chl-$a^{(Clim)}$, i.e.,

$$\Delta rChl\text{-}a = \Delta Chl\text{-}a / Chl\text{-}a^{(Clim)}, \quad (2)$$

with ΔChl-a derived from Eq. (1). Again, for each month there are two Chl-$a^{(Clim)}$ reference data for covering the time period of days 1–14 and days 15 to the end of the month. It should be noted that from Eq. (2) ΔrChl-a value is always ≥ -1, and it reaches –1 when Chl-a is 0 mg m^{-3}.

Therefore, Chl-a anomaly products of ΔChl-a and ΔrChl-a can be routinely produced in Level-2 pixel-by-pixel basis from VIIRS-derived global ocean color data. However, it is more efficient and flexible to generate global Level-3 Chl-a anomaly products from satellite-derived global Level-3 Chl-a data. In particular, VIIRS global Level-3 daily Chl-a data are routinely generated with spatial resolutions of 2-km and 9-km, and therefore it is more efficient to generate global Level-3 Chl-a anomaly products (i.e., ΔChl-a and ΔrChl-a) from VIIRS-derived Level-3 Chl-a data. The implementation of the global Chl-a anomaly products (ΔChl-a and ΔrChl-a) is described in the next section.

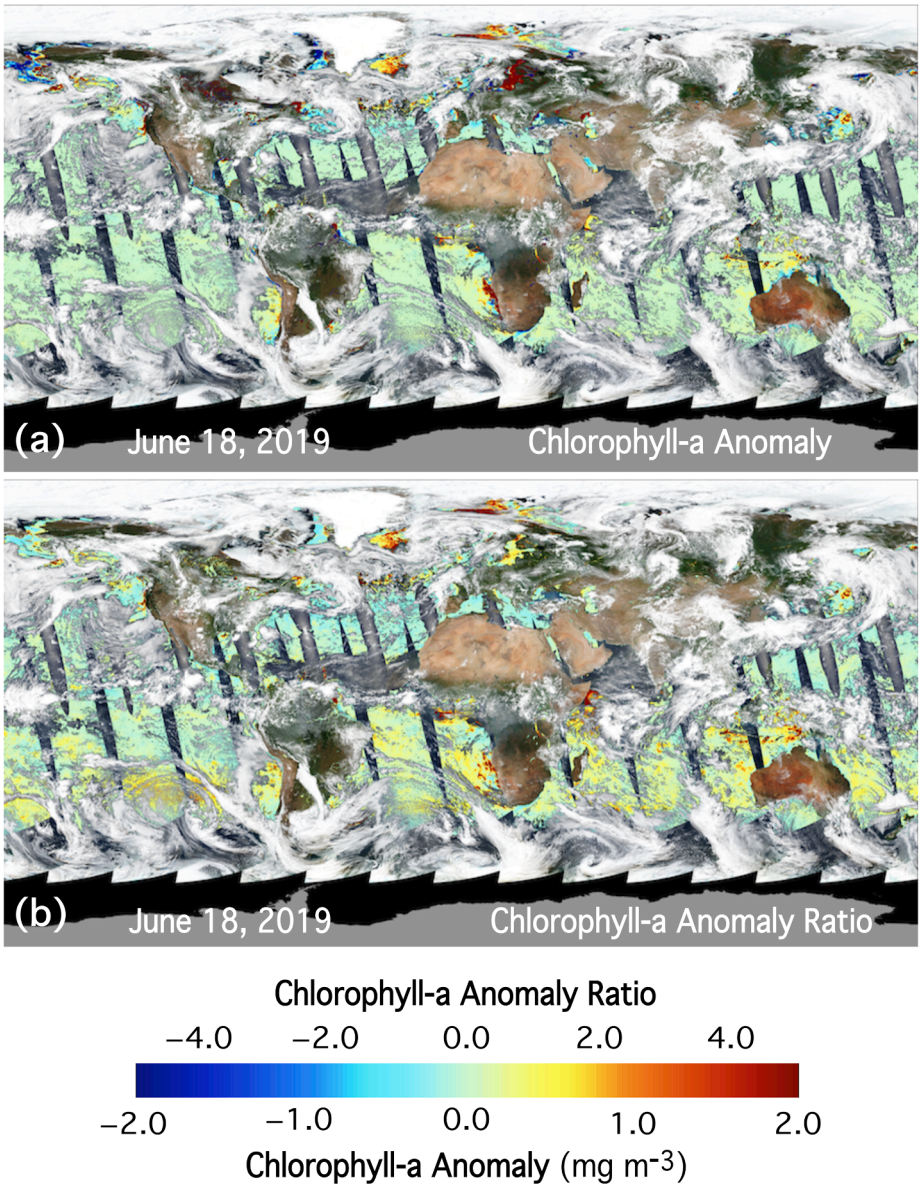

Fig. 1. VIIRS-SNPP-measured global Chl-*a* anomaly imagery of (a) Δ Chl-*a* and (b) Δ*r*Chl-*a* from data acquired on June 18, 2019. The true color image is used as a background, showing land, clouds, and data gaps with various unfavorable conditions for accurate ocean color retrievals, e.g., regions with high sun glint, large sensor-zenith angles, etc.

2.3. Implementation of the global Chl-a anomaly data processing

The global Level-3 Chl-*a* data from VIIRS have been routinely produced based on the VIIRS-measured Level-2 Chl-*a* data using the MSL12 data processing system (Wang et al., 2013). The VIIRS global ocean color Level-3 data are generated using essentially the same Level-3 satellite data processing algorithm for producing other global Level-3 ocean color products (e.g., SeaWiFS and MODIS) (Campbell et al., 1995). Specifically, in the VIIRS Level-3 ocean color data processing, pixels containing valid Level-2 ocean color data are mapped to a fixed spatial grid with a given spatial resolution (e.g., 2-km or 9-km). The grid elements or bins are arranged in rows in the data file beginning at the South Pole and ending at the North Pole. In fact, each row starts at 180° longitude and circumscribes Earth at a given latitude (Campbell et al., 1995). Therefore, the VIIRS Level-3 bin file contains data rows from Earth's South Pole to North Pole with each bin including statistics from VIIRS Level-2 data.

Using VIIRS Level-3 daily Chl-*a* data (2-km or 9-km), Level-3 61-day Chl-*a* climatology Chl-$a^{(Clim)}$ data can be derived through temporary data binning using the proper 61-day Level-3 Chl-*a* data as discussed previously. The global Level-3 Chl-*a* anomaly products of Δ Chl-*a* and Δ*r*Chl-*a* can then be calculated using VIIRS-derived Level-3 daily Chl-*a* data and Level-3 climatology Chl-$a^{(Clim)}$ data, which are generated in both 2-km and 9-km spatial resolutions. In fact, the global Level-3 Chl-*a* anomaly data processing is quite efficient, and the NRT global Chl-*a* anomaly product imageries have been routinely generated and displayed on the NOAA Ocean Color Team website through OCView (Mikelsons and Wang, 2018) since the beginning of the VIIRS mission. Indeed, it usually takes about 10 minutes to complete the global daily VIIRS Chl-*a* anomaly data processing, including the generation of all corresponding global Δ Chl-*a* and Δ*r*Chl-*a* imageries.

3. Results

VIIRS-measured global daily Δ Chl-*a* and Δ*r*Chl-*a* products are being routinely produced in the spatial resolutions of 2-km and 9-km for

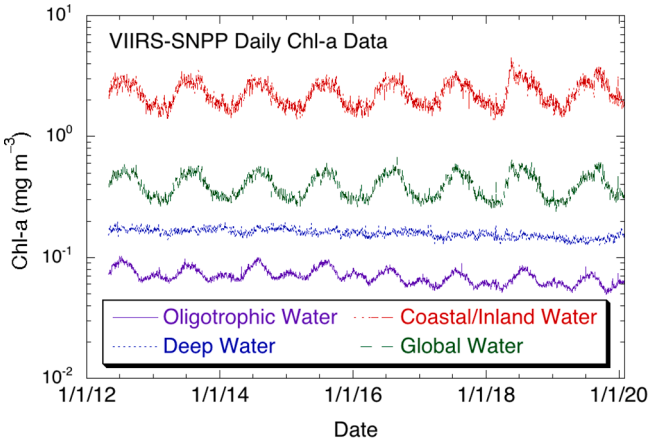

Fig. 2. VIIRS-SNPP-measured daily Chl-*a* time series (2012–2019) for global oligotrophic waters, deep waters (water depth > 1-km), coastal/inland waters (water depth ≤ 1-km), and global waters (including all oceans and coastal/inland waters).

accommodating both large/global scale and regional coverage. In fact, Chl-*a* anomaly product data have shown some importance in applications for detecting algae blooms and HABs over various coastal and inland waters. In this section, several examples are provided and discussed to demonstrate applications and usefulness of these products.

3.1. Global daily Chl-a anomaly products

We first provide an example of global Δ Chl-*a* and Δ*r*Chl-*a* imageries derived from VIIRS-SNPP Level-3 ocean color data on June 18, 2019, shown in Fig. 1a and 1b, respectively. In Fig. 1, the true color image is used as a background which displays VIIRS-SNPP observed land, ice, clouds, heavy aerosols, data gaps due to high sun glint contamination, and large solar- and/or sensor-zenith angles, as well as cases with atmospheric correction failure preventing ocean color data retrievals (Mikelsons and Wang, 2019; Mikelsons et al., 2020). It is noted that data gaps of Δ Chl-*a* and Δ*r*Chl-*a* in Fig. 1 are indicated in black.

On June 18, 2019, while the vast open oceans in Fig. 1 show few areas of elevated Chl-*a*, many coastal and inland water regions experienced algae blooms during the boreal summer. At the global scale, the two metrics in Δ Chl-*a* and Δ*r*Chl-*a* (Fig. 1a and 1b) are quite similar. However, some significant differences are evident in the global Δ Chl-*a* and Δ*r*Chl-*a* imageries. For example, Δ Chl-*a* were generally very high in the Baltic Sea, indicating continued expanding algae blooms. On the other hand, Δ*r*Chl-*a* data in the region were relatively small, implying that the recent increase in Chl-*a* is insignificant compared to the overall high Chl-*a* levels reached during the earlier stages of this protracted bloom event. In another example, an area in the West Indian Ocean near the coast of Somalia exhibited a moderate increase in Δ Chl-*a*, but Δ*r*Chl-*a* values were quite high in this likely upwelling-induced bloom. In fact, many areas in the Northern Hemisphere experienced summer algae blooms in part due to ample sunlight, while Antarctica and the surrounding areas were under polar night. There are many similarities in Δ Chl-*a* and Δ*r*Chl-*a* imagery, but the latter is a better indicator for the relative strength of the algae bloom intensity.

It should be noted that, although Δ*r*Chl-*a* data are always ≥ –1, we have used the scales that are appropriate to that of Δ Chl-*a* for easy comparison and visualization. This is also true for other quantitative plots in the next several sections. In fact, for Chl-*a* anomaly products, we are mainly focusing on the anomalous high Chl-*a* values for detecting algae blooms.

3.2. Time series of global daily Chl-a and Chl-a anomaly products

For quantitative presentation and evaluation of global Chl-*a* temporal distributions, Fig. 2 provides VIIRS-SNPP-derived daily Chl-*a* over

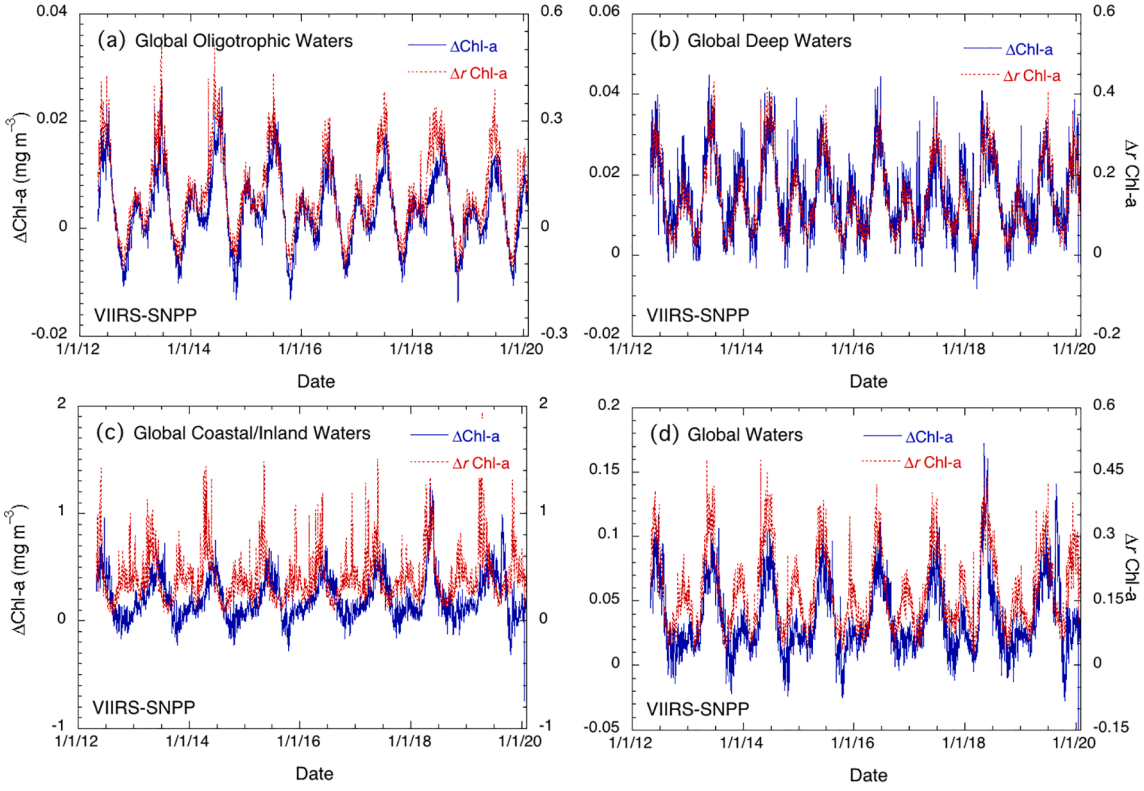

Fig. 3. VIIRS-SNPP-measured daily Δ Chl-*a* and Δ*r*Chl-*a* time series (2012–2019) over (a) global oligotrophic waters, (b) deep waters (water depth > 1-km), (c) coastal/inland waters (water depth ≤ 1-km), and (d) global waters. Note that the left-side y-axis is for Δ Chl-*a* and right-side y-axis is for Δ*r*Chl-*a*.

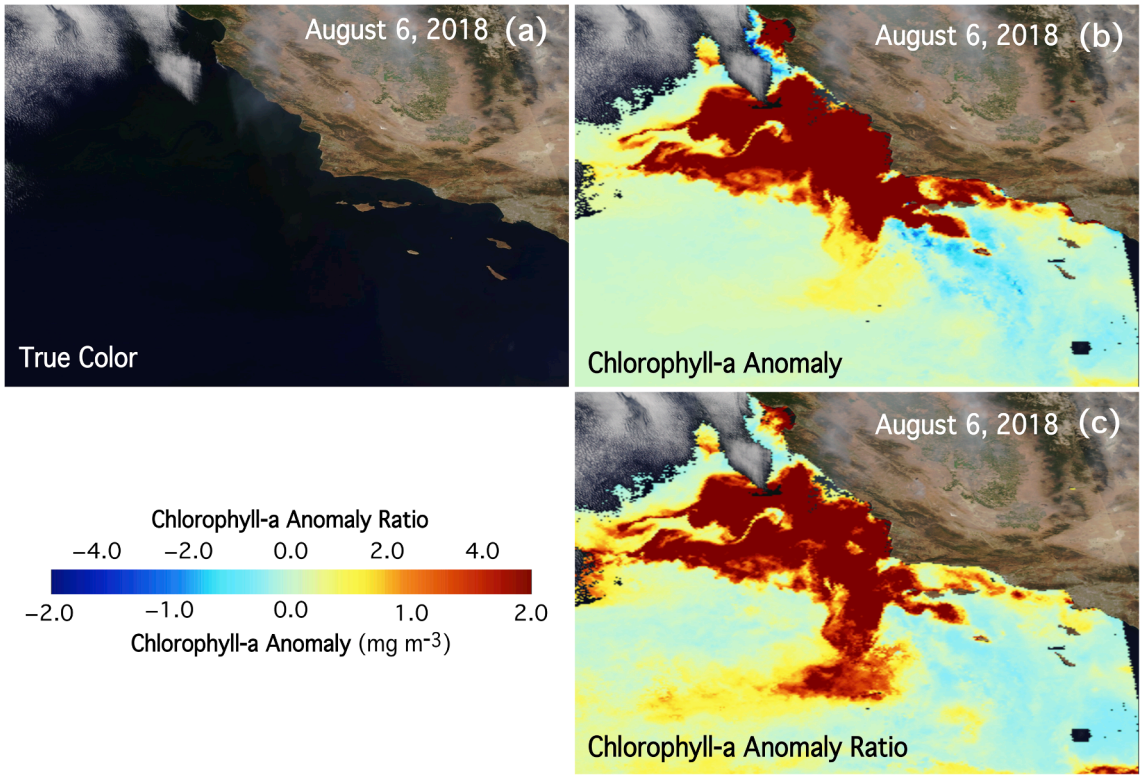

Fig. 4. VIIRS-NOAA-20-measured (a) true color image, (b) ΔChl-*a*, and (c) ΔrChl-*a* data acquired on August 6, 2018, over the coast of California. The massive algae bloom seen in the center of the image is almost identical in both ΔChl-*a* and ΔrChl-*a* imagery, yet there are differences in coastal areas. Further out in the open ocean (lower part of the image), ΔrChl-*a* is more sensitive due to a lower background (i.e., reference Chl-$a^{(Clim)}$) Chl-*a* values.

global oligotrophic waters, deep waters (water depth >1-km), coastal/inland waters (i.e., regions with water depth ≤ 1-km), and global waters (including all oceans and coastal/inland waters). These Chl-*a* data cover the VIIRS-SNPP mission from 2012 to 2019. As expected, Chl-*a* values for these water regions change from low values for oligotrophic water with a median value of ~0.07 mg m^{-3}, to a slightly high median value for deep waters of ~0.15 mg m^{-3}, and a high median Chl-*a* value for coastal/inland waters of ~2.03 mg m^{-3}. The median global daily Chl-*a* value (covering all oceans and inland waters) is ~0.35 mg m^{-3} from VIIRS-SNPP measurements (Fig. 2).

These global Chl-*a* time series data show some obvious seasonal and interannual variations. Specifically, over the global oligotrophic waters (i.e., North and South Pacific Ocean gyres, North and South Atlantic Ocean gyres, and South Indian Ocean gyre), there are two Chl-*a* peaks annually with large one at boreal summer and small one at boreal winter. In fact, both Chl-*a* peaks represent significant Chl-*a* increase in the local winter season, one in the south (Australia winter) and another in the north (boreal winter), due to the strong winter water vertical mixing that drives the increased phytoplankton biomass (Signorini et al., 2015). However, for the global deep water Chl-*a* time series, there are minimum seasonal variations (not obvious visually), although one can see some variations with a careful inspection. For Chl-*a* time series over global coastal/inland waters (red in Fig. 2), seasonal variation is quite clear with Chl-*a* peaks in the boreal summer and troughs in boreal winter. However, although not obvious, one still can see some small Chl-*a* peak in boreal winter for Chl-*a* time series over global coastal/inland waters in Fig. 2.

In comparison to Fig. 2, Fig. 3 provides Chl-*a* anomaly time series for ΔChl-*a* and ΔrChl-*a* over global oligotrophic waters (Fig. 3a), deep waters (Fig. 3b), coastal/inland waters (Fig. 3c), and global waters (Fig. 3d). In Fig. 3, the left-side y-axis indicates the scale of ΔChl-*a*, while the right-side y-axis shows the scale of ΔrChl-*a*. It is noted that the scales of ΔChl-*a* are significantly different for different global ocean regions,

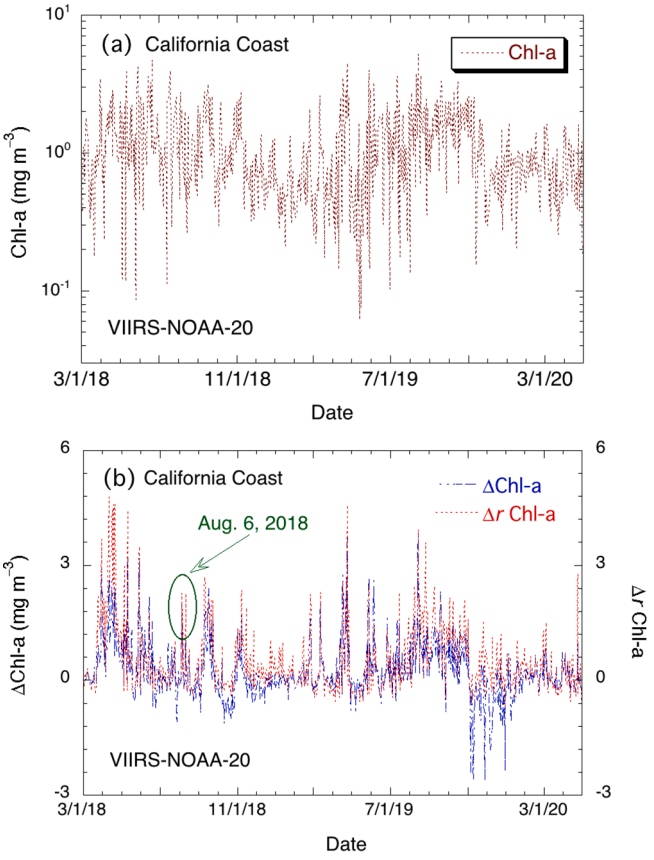

Fig. 5. VIIRS-NOAA-20-measured daily time series (March 2018–May 2020) of (a) Chl-*a* and (b) ΔChl-*a* and ΔrChl-*a* over the coast of California (region shown in Fig. 4).

with ΔChl-*a* generally within ~0.02 mg m^{-3}, ~0.04 mg m^{-3}, ~1.0 mg m^{-3}, and ~0.1 mg m^{-3}, for global oligotrophic waters, deep waters, coastal/inland waters, and global waters, respectively. On the other hand, the scales of Δ*r*Chl-*a* are similar for global oligotrophic waters, deep waters, and global waters at ~0.5, ~0.4, and ~0.5, respectively, while it is ~1.5 for global coastal/inland waters. Fig. 3 shows that Chl-*a* variations are really highlighted in Chl-*a* anomaly products (ΔChl-*a* and Δ*r*Chl-*a*) for global oceans and coastal/inland waters, e.g., one can now see clearly two Chl-*a* peaks (one in boreal winter and another in Australia winter) in global deep waters (Fig. 3b). It should also be noted that, for global oligotrophic waters and deep waters, both ΔChl-*a* and Δ*r*Chl-*a* are quite consistent (Fig. 3a and b), although values for these two differ. However, for global coastal/inland waters, there are some slightly different times in peak values for ΔChl-*a* and Δ*r*Chl-*a* (Fig. 3c), showing that ΔChl-*a* and Δ*r*Chl-*a* may represent different stages in algae biomass variations and can be used for understanding of the Chl-*a* changes in the region.

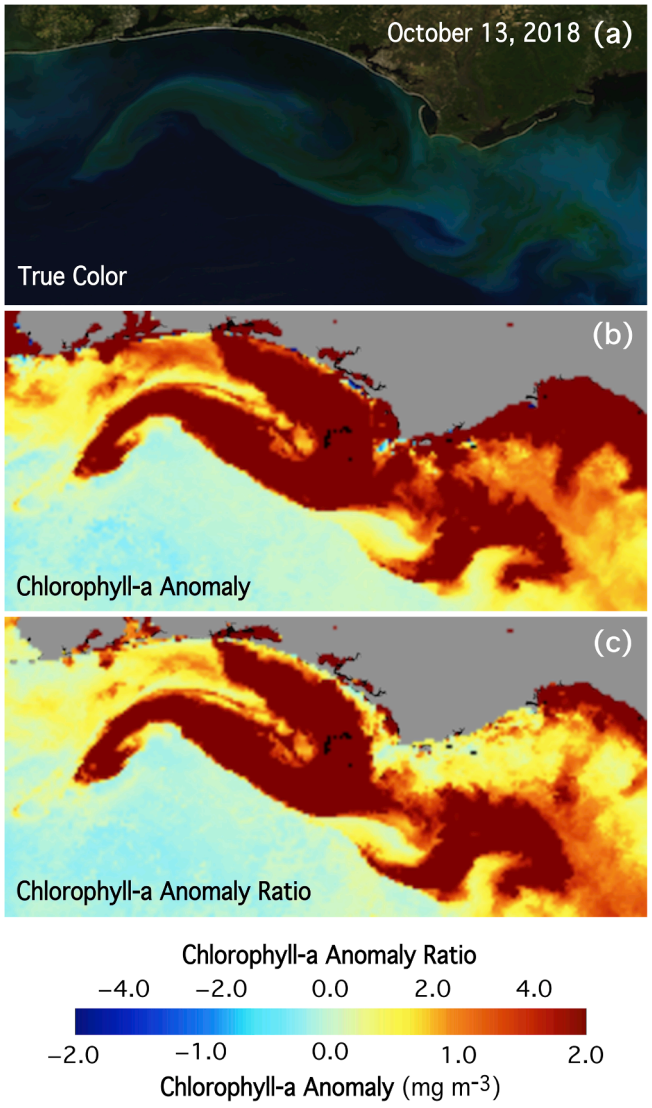

Fig. 6. VIIRS-NOAA-20-measured (a) true color image, (b) ΔChl-*a*, and (c) Δ*r*Chl-*a* from data acquired on October 13, 2018, over the GOM region, showing the coast of western Florida days after the hurricane Michael passed the area. Plumes of river discharge into the gulf carrying high amounts of sediment and nutrients were shaped by the gulf currents. Both ΔChl-*a* and Δ*r*Chl-*a* showed sudden and very strong increases of Chl-*a* in these areas.

3.3. Examples of daily Chl-a anomaly products from coastal regions

3.3.1. The coast of California

As seen from the global imagery and quantitative time series of Chl-*a* anomaly products in the previous section (Figs. 1–3), both ΔChl-*a* and Δ*r*Chl-*a* data can be used to characterize biological productivity in global open oceans and coastal/inland waters. In Fig. 4, we show a scene over the west coast of California, captured by VIIRS-NOAA-20 on August 6, 2018 (Fig. 4a for true color image), showing features of a widespread algae bloom in both ΔChl-*a* (Fig. 4b) and Δ*r*Chl-*a* (Fig. 4c) images. While ΔChl-*a* were high in most adjacent coastal regions, areas with high Δ*r*Chl-*a* were more selective, highlighting only the regions with the most significant relative increase in Chl-*a*. Further out in the open ocean, however, Δ*r*Chl-*a* were more sensitive to uncover gradual increases in Chl-*a* relative to lower Chl-*a* baseline (i.e., reference Chl-$a^{(Clim)}$) values in the water. Obviously, in this case, high ΔChl-*a* and Δ*r*Chl-*a* values are mostly overlapped in the region. However, we do see some differences in high ΔChl-*a* and Δ*r*Chl-*a* coverage in the region.

Fig. 5 shows regional quantitative Chl-*a* and Chl-*a* anomalies (ΔChl-*a* and Δ*r*Chl-*a*) over the west coast of California from VIIRS-NOAA-20 mission-long observations. For the region, Chl-*a* data show some seasonal variation with Chl-*a* peaks at the boreal summer (Fig. 5a). However, VIIRS-NOAA-20-derived Chl-*a* data in the region have high variability with its mean, median, and standard deviation (STD) values of ~1.14 mg m^{-3}, ~0.92 mg m^{-3}, and ~0.78 mg m^{-3}, respectively. On the other hand, Chl-*a* anomaly data in Fig. 5b show some high Chl-*a* cases, in particular, Δ*r*Chl-*a* data provide clear abnormal Chl-*a* cases in the region. Specifically, the bloom event in the region on August 6, 2018, which is shown in Fig. 4, is noted in Fig. 5b. The mean, median, and STD values for ΔChl-*a* in the region from VIIRS-NOAA-20 mission-

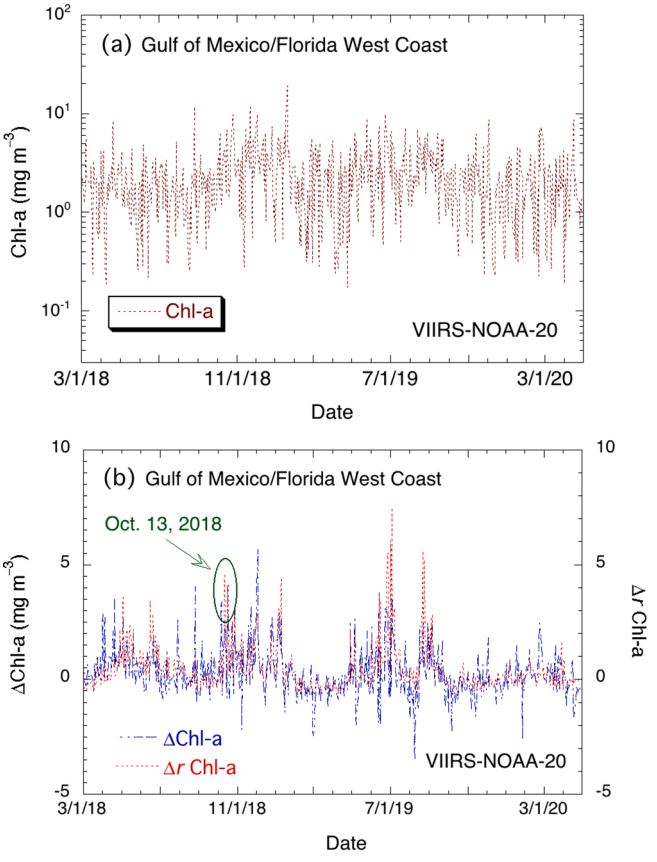

Fig. 7. VIIRS-NOAA-20-measured daily time series (March 2018–May 2020) of (a) Chl-*a* and (b) ΔChl-*a* and Δ*r*Chl-*a* over the Gulf of Mexico and coast of western Florida (region shown in Fig. 6).

long data are ~0.23 mg m^{-3}, ~0.07 mg m^{-3}, and ~0.74 mg m^{-3}, respectively, while mean, median, and STD values for ΔrChl-*a* in the region are ~0.51, ~0.24, and ~0.88, respectively. Thus, results of ΔrChl-*a* show mean Chl-*a* variation in the region about 51%, significantly higher than normal for identifying such abnormal cases using ΔrChl-*a* data.

3.3.2. *The Gulf of Mexico and coast of western Florida*

In another example featuring the coastal areas, we show the GOM and coast of western Florida in the aftermath of the hurricane Michael as seen from VIIRS-NOAA-20 on October 13, 2018 (Fig. 6). Indeed, Fig. 6 shows the result of a sudden increase of the river discharge following the rains brought large plumes of fresh water rich in nutrients into the GOM region (Shi and Wang, 2009b). These plumes represent conditions for a rapid algae growth, as indicated by elevated levels of Chl-*a* values both in absolute and relative terms, as evident from ΔChl-*a* (Fig. 6b) and ΔrChl-*a* (Fig. 6c) imagery. In fact, the bloom feature in Fig. 6b and 6c corresponds well with the true color image in Fig. 6a.

Quantitative characterization of the biomass activity in the region can be described with Chl-*a* and Chl-*a* anomaly (ΔChl-*a* and ΔrChl-*a*) time series in Fig. 7. Chl-*a* time series derived from VIIRS-NOAA-20 mission-long measurements is provided in Fig. 7a, while ΔChl-*a* and ΔrChl-*a* time series data are shown in Fig. 7b. Again, we see high Chl-*a* variations from VIIRS-NOAA-20 daily measurements (Fig. 7a) with mean, median, and STD values of ~2.47 mg m^{-3}, ~2.17 mg m^{-3}, and ~1.87 mg m^{-3}, respectively. Although not very clear from Chl-*a* data, there are Chl-*a* peaks in the boreal summer in the region. On the other hand, Chl-*a* anomaly products, particularly ΔrChl-*a* data, show clear peaks in the boreal summer, with additional peak values in the boreal winter (Fig. 7b). There are also some anomaly Chl-*a* peaks in various individual cases, clearly identified by ΔChl-*a* and ΔrChl-*a* data. Particularly, the high bloom event in the region on October 13, 2018 (Fig. 6), is noted in Fig. 7b. For the GOM and coast of western Florida region in Fig. 6, the VIIRS-NOAA-20-derived mean, median, and STD values for ΔChl-*a* are ~0.29 mg m^{-3}, ~0.12 mg m^{-3}, and ~1.08 mg m^{-3}, respectively, while mean, median, and STD values for ΔrChl-*a* are ~0.43, ~0.15, and ~1.01, respectively. Therefore, significant variations are again shown in ΔrChl-*a* with a mean value of ~43%. It is noted that from results in Fig. 7b the Chl-*a* anomaly products ΔChl-*a* and ΔrChl-*a* show different strength and magnitudes for Chl-*a* anomaly events, and can be used to provide more complete information of biomass activity in the region.

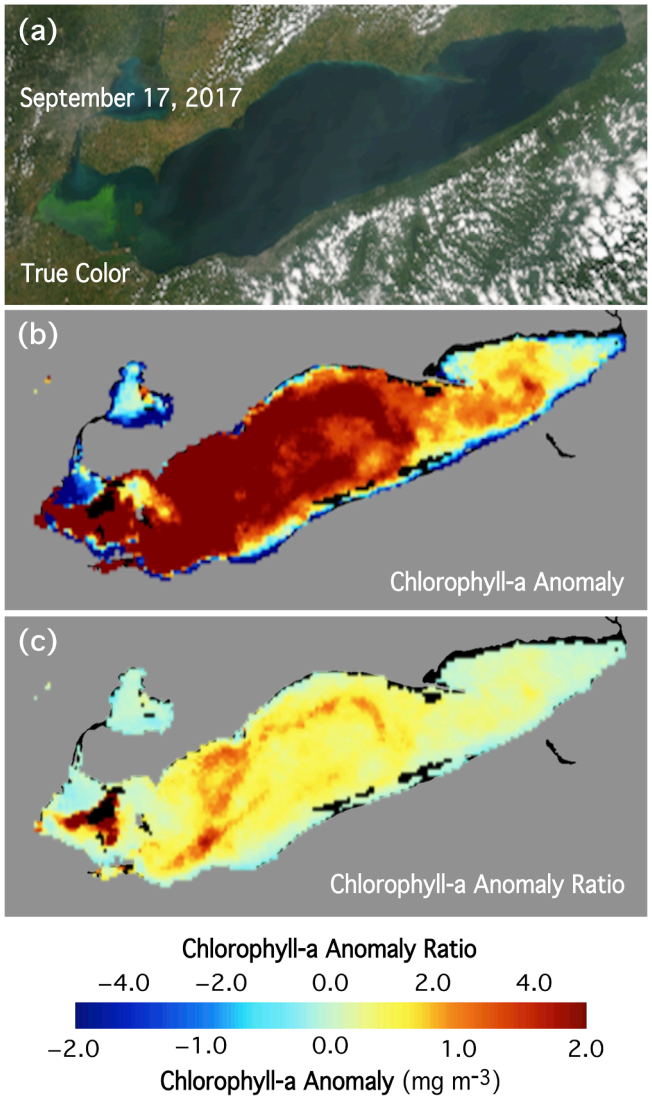

Fig. 8. VIIRS-SNPP-measured (a) true color imagery, (b) ΔChl-*a*, and (c) ΔrChl-*a* on September 17, 2017, over Lake Erie. While the ΔChl-*a* showed a significant increase in most parts of the lake, the Chl-*a* anomaly in relative difference ΔrChl-*a* highlighted the areas with the most intense blooms, which are also evident in the true color imagery.

3.4. *Chl-a anomaly products from Lake Erie*

Chl-*a* anomaly products (ΔChl-*a* and ΔrChl-*a*) are also quite useful for detecting and analyzing algae blooms over global inland waters. In particular, Chl-*a* anomaly ratio product ΔrChl-*a* can be especially helpful. Fig. 8 shows the summer algae blooms in Lake Erie on July 28, 2017, which were acquired by VIIRS-SNPP. As expected, ΔChl-*a* in Fig. 8b shows that Chl-*a* levels were elevated in most parts of the lake during the

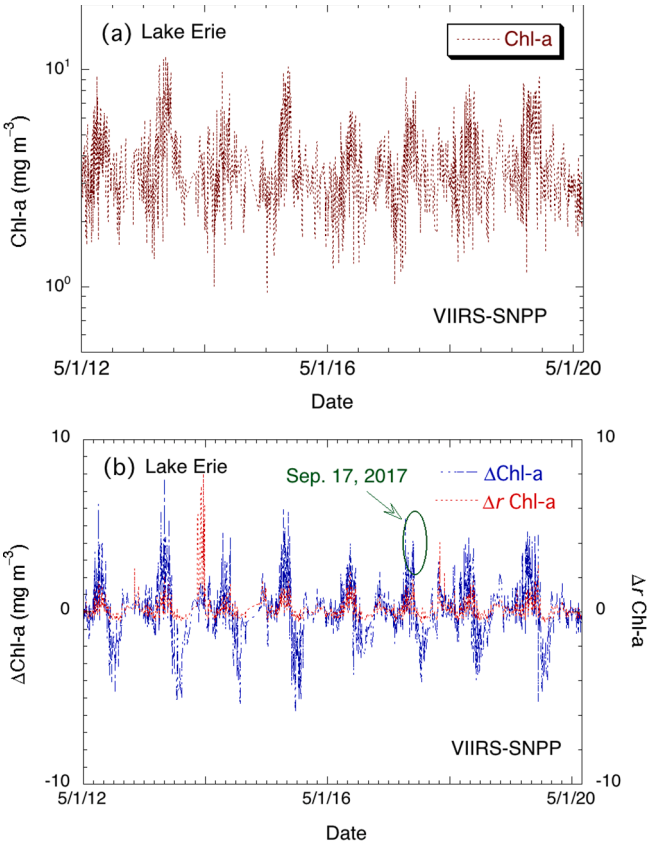

Fig. 9. VIIRS-SNPP-measured daily time series (May 2012–May 2020) of (a) Chl-*a* and (b) ΔChl-*a* and ΔrChl-*a* over Lake Erie in the US (region shown in Fig. 8).

boreal summer. However, in Fig. 8c, anomaly ratio product ΔrChl-*a* shows fewer areas where the relative increase of Chl-*a* was significant. Indeed, comparing result in Fig. 8c to the true color imagery in Fig. 8a, we note a nearly perfect correspondence with bright green algae blooms in the west and central parts of the lake. Therefore, in this case, the Chl-*a* anomaly ratio (or relative difference) product ΔrChl-*a* provided more useful information to identify locations of algae blooms in the lake.

Time series in Chl-*a* and Chl-*a* anomalies from VIIRS-SNPP mission-long observation for Lake Erie are provided in Fig. 9. Chl-*a* time series in Fig. 9a shows seasonal variations in Lake Erie with Chl-*a* peaks in the boreal summer, consistent with usual algae blooms (or HABs) during the summer in the lake (Michalak et al., 2013; Steffen et al., 2014; Watson et al., 2016). In addition, there are also modeling efforts in western Lake Erie to understand and quantify the drivers for the phytoplankton dynamics (Jiang et al., 2015). From VIIRS-SNPP mission-long measurements, the mean, median, and STD Chl-*a* values in Lake Erie are ~3.75 mg m^{-3}, ~3.37 mg m^{-3}, and ~1.56 mg m^{-3}, respectively. Time series of ΔChl-*a* and ΔrChl-*a* from VIIRS-SNPP mission-long measurements in Lake Erie are quite consistent (Fig. 9b), although ΔChl-*a* and ΔrChl-*a* show some different data strengths, emphasizing on the biomass activities differently in the region. Indeed, statistics for ΔChl-*a* in the lake from VIIRS-SNPP observations have mean, median, and STD values of about 0.20 mg m^{-3}, 0.15 mg m^{-3}, and 1.67 mg m^{-3}, respectively, while the corresponding ΔrChl-*a* statistical values are about 0.24, 0.08, and 0.79, respectively. It is interesting to note that mean and median ΔChl-*a* are relatively small, while the STD value is quite significant, indicating the biomass variation in the lake is quite high (e.g., driven by the eventful algae blooms). This is also reflected in the statistical results of ΔrChl-*a* with about mean value of 24%, small median value of 0.08, and STD value of 0.79. Again, in Fig. 9b, the high algae bloom event on September 17, 2017, is marked.

3.5. Using ΔrChl-*a* in characterizing of the cyclone Cebile

We show another example how the Chl-*a* anomaly ratio (or relative difference) ΔrChl-*a* can be useful on the open ocean for detecting the surface features. Fig. 10 shows VIIRS-SNPP-derived ΔChl-*a* and ΔrChl-*a* images in the Indian Ocean in the area visited by the tropical cyclone Cebile on February 6, 2018. The storm path is shown with blue circles in Fig. 10b, with circle radii proportional to the wind speeds. The ΔChl-*a* image, displayed in Fig. 10a, does not show significant increase above the Chl-*a* baseline values (Chl-$a^{(Clim)}$) obviously, consistent with the normally low productivity in the ocean gyres. However, the ΔrChl-*a* image, as presented in Fig. 10b, shows a circular pattern of increased Chl-*a* in the area where the tropical cyclone Cebile attained its maximum wind speeds. Indeed, the ocean regions visited by the storm at its maximum strength and subject to the highest wind speeds from January 31–February 3, 2018, showed a significant increase in ΔrChl-*a* compare with those from other regions (Fig. 10b). The increase of Chl-*a* during the cyclone overpass was due to intensive mixing brought by the strong wind stress (Babin et al., 2004; Lin et al., 2003; Liu et al., 2009; Miller et al., 2006; Shi and Wang, 2007). The deepened mix layer brought up the nutrients originally below the mixed-layer to the surface and facilitated Chl-*a* growth there (Liu et al., 2009). There was also moderate elevated Chl-*a* along the track of the cyclone pass that can only be observed from the ΔrChl-*a* imagery (Fig. 10b). Thus, the Chl-*a* anomaly ratio ΔrChl-*a* can be used to identify changes in the open ocean that are small by magnitude, but still significant relative to the normally low Chl-*a* levels in these waters.

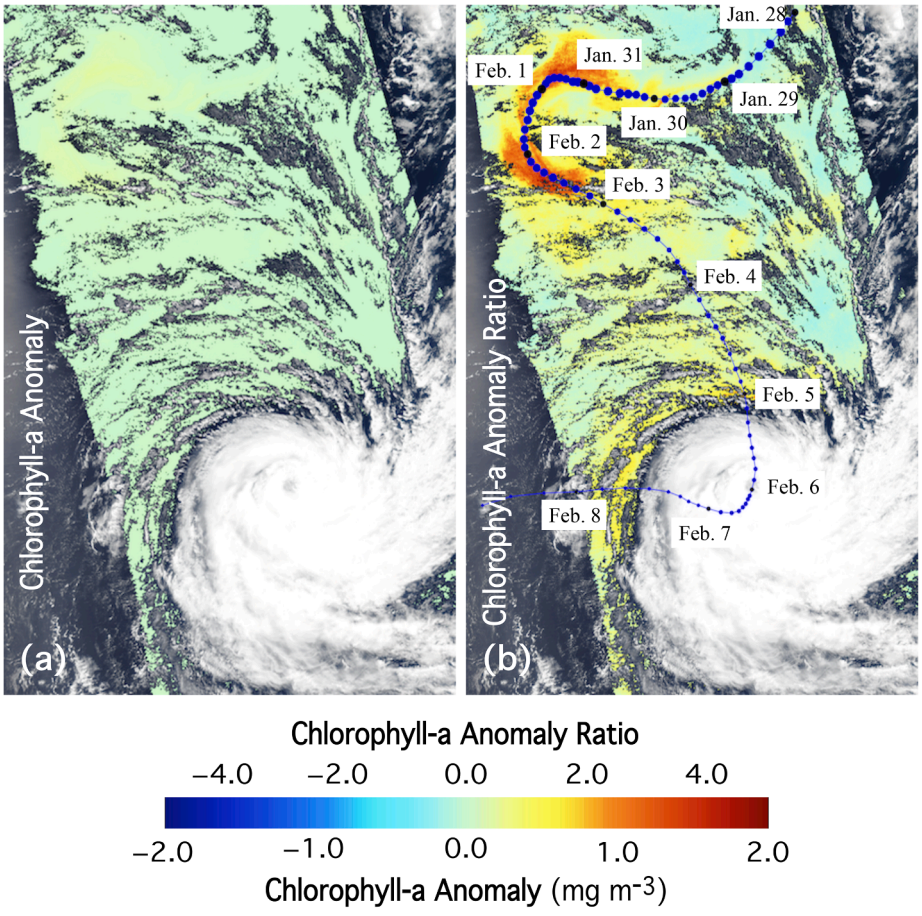

Fig. 10. VIIRS-SNPP-measured (a) ΔChl-*a* and (b) ΔrChl-*a* from data acquired on February 6, 2018, over the Indian Ocean where the area was visited by the tropical cyclone Cebile. The VIIRS true color imagery is used as a background in both panels and shows the cyclone with a distinguishable eye in the lower parts of the panels.

4. Discussions and conclusion

In this study, we introduced two new VIIRS global Level-3 Chl-*a* anomaly products, Chl-*a* anomaly in difference *Δ*Chl-*a* and Chl-*a* anomaly ratio (or its relative difference) *Δr*Chl-*a*, as well as described how they are defined, calculated, and implemented in the satellite ocean color data processing system. Essentially, *Δ*Chl-*a* data are defined as the same as those developed by the NOAA HABs group (Stumpf, 2001; Stumpf et al., 2003; Tomlinson et al., 2004), while the *Δr*Chl-*a* data are calculated as Chl-*a* relative difference as compared to a reference Chl-$a^{(Clim)}$. Detailed Chl-$a^{(Clim)}$ computations in the ocean color data processing are described and discussed. Indeed, it is important to calculate appropriate Chl-*a* reference Chl-$a^{(Clim)}$ data for deriving reasonable *Δ*Chl-*a* and *Δr*Chl-*a* products. It is noted that the accuracy of *Δ*Chl-*a* and *Δr*Chl-*a* products should be generally less sensitive to the accuracy of satellite-derived Chl-*a* data, as the computation involves subtraction or division for removing some Chl-*a* errors. Therefore, the Chl-*a* anomaly products should be reasonably accurate. The two Chl-*a* anomaly products, *Δ*Chl-*a* and *Δr*Chl-*a*, are being routinely produced daily with related global images generated and distributed from the NOAA Ocean Color Team website (https://www.star.nesdis.noaa.gov/socd/mecb/color/), and they can be easily accessed using the web-based visualization tool OCView (Mikelsons and Wang, 2018). In addition, both *Δ*Chl-*a* and *Δr*Chl-*a* global data are now being freely distributed through NOAA CoastWatch (https://coastwatch.noaa.gov/cw/index.html).

Using VIIRS-SNPP and VIIRS-NOAA-20 ΔChl-*a* and *Δr*Chl-*a* imageries, as well as some detailed quantitative seasonal and interannual analyses, we presented several examples over the locations including global, coastal, and inland waters to show some applications and usefulness of the two Chl-*a* anomaly products. Our results have shown that values of global *Δ*Chl-*a* and *Δr*Chl-*a* data can be used to effectively detect algae bloom events over open oceans and coastal/inland waters. In particular, the new *Δr*Chl-*a* product can often identify more precise regions with significantly increased Chl-*a* values, and even detect an open ocean Chl-*a* bloom missed by the anomaly *Δ*Chl-*a* data due to relatively low Chl-*a* values in open oceans, or undiscernible from extended areas of elevated Chl-*a* anomaly due to large background Chl-*a* values. Therefore, with both *Δ*Chl-*a* and *Δr*Chl-*a* data, global abnormal algae biomass events can be more reliably identified and detected. With such global daily Chl-*a* variation information, specific regional Chl-*a* abnormal biomass activities can be further investigated and studied using other satellite measurements (e.g., high spatial and/or hyperspectral data for a focused regional study).

Declaration of Competing Interest

The authors declare that they have no known competing financial interests or personal relationships that could have appeared to influence the work reported in this paper.

Acknowledgments

This work was supported by the Joint Polar Satellite System (JPSS) funding. We thank two anonymous reviewers for their useful comments. The scientific results and conclusions, as well as any views or opinions expressed herein, are those of the author(s) and do not necessarily reflect those of NOAA or the Department of Commerce.

References

Babin, S.M., Carton, J.A., Dickey, T.D., Wiggert, J.D., 2004. Satellite evidence of hurricane-induced phytoplankton blooms in an oceanic desert. J. Geophys. Res. 109, C03043. https://doi.org/10.1029/2003JC001938.

Barnes, B.B., Cannizzaro, J.P., English, D.C., Hu, C., 2019. Validation of VIIRS and MODIS reflectance data in coastal and oceanic waters: an assessment of methods. Remote Sens. Environ. 220, 110–123.

Campbell, J.W., Blaisdell, J.M., Darzi, M., 1995. Level-3 SeaWiFS data products: spatial and temporal binning algorithms. In: Hooker, S.B., Firestone, E.R., Acker, J.G. (Eds.), NASA Goddard Space Flight Center. Greenbelt, Maryland.

Donlon, C., Berruti, B., Buongiorno, A., Ferreira, M.-H., Femenias, P., Frerick, J., Goryl, P., Klein, U., Laur, H., Mavrocordatos, C., Nieke, J., Rebhan, H., Seitz, B., Stroede, J., Sciarra, R., 2012. The global monitoring for environment and security (GMES) sentinel-3 mission. Remote Sens. Environ. 120, 37–57.

Esaias, W.E., Abbott, M.R., Barton, I., Brown, O.B., Campbell, J.W., Carder, K.L., Clark, D.K., Evans, R.L., Hodge, F.E., Gordon, H.R., Balch, W.P., Letelier, R., Minnet, P.J., 1998. An overview of MODIS capabilities for ocean science observations. IEEE Trans. Geosci. Remote Sens. 36, 1250–1265.

Goldberg, M.D., Kilcoyne, H., Cikanek, H., Mehta, A., 2013. Joint Polar Satellite System: The United States next generation civilian polar-orbiting environmental satellite system. J. Geophys. Res. Atmos. 118, 13463–13475. https://doi.org/10.11002/12013JD020389.

Gordon, H.R., Clark, D.K., Mueller, J.L., Hovis, W.A., 1980. Phytoplankton pigments from the nimbus-7 coastal zone color scanner: comparisons with surface measurements. Science 210, 63–66.

Gordon, H.R., Wang, M., 1994. Retrieval of water-leaving radiance and aerosol optical thickness over the oceans with SeaWiFS: a preliminary algorithm. Appl. Opt. 33, 443–452.

Gower, J., King, S., Borstad, G., Brown, L., 2005. Detection of intense plankton blooms using the 709 nm band of the MERIS imaging spectrometer. Int. J. Remote Sens. 26, 2005–2012.

Gower, J., King, S., Goncalves, P., 2008. Global monitoring of plankton blooms using MERIS MCI. Int. J. Remote Sens. 29, 6209–6216.

Groom, S., Sathyendranath, S., Ban, Y., Bernard, S., Brewin, R., Brotas, V., Brockmann, C., Chauhan, P., Choi, J., Chuprin, A., Ciavatta, S., Cipollini, P., Donlon, C., Franz, B.A., He, X., Hirata, T., Jackson, T., Kampel, M., Krasemann, H., Lavender, S.J., Pardo-Martinez, S., Melin, F., Platt, T., Santoleri, R., Skakala, J., Schaeffer, B., Smith, M., Steinmeta, F., Valente, A., Wang, M., 2019. Satellite ocean colour: current status and future perspective. Front. Mar. Sci. 6, 485. https://doi.org/10.3389/fmars.2019.00485.

Hlaing, S., Harmel, T., Gilerson, A., Foster, R., Weidemann, A., Arnone, R., Wang, M., Ahmed, S., 2013. Evaluation of the VIIRS ocean color monitoring performance in coastal regions. Remote Sens. Environ. 139, 398–414.

Hovis, W.A., Clark, D.K., Anderson, F., Austin, R.W., Wilson, W.H., Baker, E.T., Ball, D., Gordon, H.R., Mueller, J.L., Sayed, S.T.E., Strum, B., Wrigley, R.C., Yentsch, C.S., 1980. Nimbus 7 Coastal Zone Color Scanner: system description and initial imagery. Science 210, 60–63.

Hu, C., 2009. A novel ocean color index to detect floating algae in the global oceans. Remote Sens. Environ. 113, 2118–2129.

Hu, C., Barnes, B.B., Feng, L., Wang, M., Jiang, L., 2020. On the interplay between ocean color data quality and data quantity: impacts of quality control flags. IEEE Geosci. Remote Sens. Lett. 17, 745–749.

Hu, C., Lee, Z., Franz, B.A., 2012. Chlorophyll a algorithms for oligotrophic oceans: a novel approach based on three-band reflectance difference. J. Geophys. Res. 117, C01011. https://doi.org/10.01029/02011JC007395.

Hu, C., Li, D., Chen, C., Ge, J., Muller-Karger, F.E., Liu, J., Yu, F., He, M.X., 2010. On the recurrent Ulva prolifera blooms in the Yellow Sea and East China Sea. J. Geophys. Res. 115, C05017. https://doi.org/10.1029/2009JC005561.

IOCCG, 2008. Why ocean colour? The societal benefits of ocean-colour technology. In: Platt, T., Hoepffner, N., Stuart, V., Brown, C. (Eds.), Reports of the International Ocean-Colour Coordinating Group, IOCCG, Dartmouth, Canada.

IOCCG, 2012. Mission requirements for future ocean-colour sensors. In: McClain, C.R., Meister, G. (Eds.), Reports of the International Ocean-Colour Coordinating Group, IOCCG, Dartmouth, Canada.

IOCCG, 2018. Earth observations in support of global water quality monitoring. In: Greb, S., Dekker, A., Binding, C. (Eds.), Reports of the International Ocean-Colour Coordinating Group, IOCCG, Dartmouth, Canada.

Jiang, L., Wang, M., 2014. Improved near-infrared ocean reflectance correction algorithm for satellite ocean color data processing. Opt. Express 22, 21657–21678.

Jiang, L., Xia, M., Ludsin, S.A., Rutherford, E.S., Mason, D.M., Jarrin, J.M., Pangle, K.L., 2015. Biophysical modeling assessment of the drivers for plankton dynamics in dreissenid-colonized western Lake Erie. Ecol. Modell. 308, 18–33.

Lee, Z.P., Carder, K.L., Arnone, R.A., 2002. Deriving inherent optical properties from water color: a multiple quasi-analytical algorithm for optically deep waters. Appl. Opt. 41, 5755–5772.

Lee, Z.P., Darecki, M., Carder, K., Davis, C., Stramski, D., Rhea, W., 2005. Diffuse attenuation coefficient of downwelling irradiance: an evaluation of remote sensing methods. J. Geophys. Res. 110, C02017. https://doi.org/10.1029/2004JC002573.

Lin, I., Liu, W.T., Wu, C.-C., Wong, G.T.F., Hu, C., Che, Z., Liang, W.-D., Yang, Y., Liu, K.-K., 2003. New evidence for enhanced ocean primary production triggered by tropical cyclone. Geophy. Res. Lett. 30, 1718. https://doi.org/10.1029/2003GL017141.

Liu, X., Wang, M., 2018. Gap filling of missing data for the VIIRS global ocean color products using the DINEOF method. IEEE Trans. Geosci. Remote Sens. 56, 4464–4476.

Liu, X., Wang, M., 2019a. Filling the gaps in ocean maps. Eos Trans. AGU 100. https://doi.org/10.1029/2019EO136548.

Liu, X., Wang, M., 2019b. Filling the gaps of missing data in the merged VIIRS SNPP/NOAA-20 ocean color product using the DINEOF method. Remote Sens. 11, 178. https://doi.org/10.3390/rs11020178.

Liu, X., Wang, M., 2021. Super-resolution of VIIRS-measured ocean color products using deep convolutional neural network. IEEE Trans. Geosci. Remote Sens. 59, 114–127.

Liu, X., Wang, M., Shi, W., 2009. A study of a Hurricane Katrina-induced phytoplankton bloom using satellite observations and model simulations. J. Geophys. Res. 114, C03023. https://doi.org/10.1029/2008JC004934.
McClain, C.R., 2009. A decade of satellite ocean color observations. Annu. Rev. Mar. Sci. 1, 19–42.
McClain, C.R., Feldman, G.C., Hooker, S.B., 2004. An overview of the SeaWiFS project and strategies for producing a climate research quality global ocean bio-optical time series. Deep Sea Res. Part II 51, 5–42.
Michalak, A.M., Anderson, E.J., Beletsky, D., Boland, S., Bosch, N.S., Bridgeman, T.T., Chaffin, J.D., Cho, K., Confesor, R., Daloglu, I., DePinto, J.V., Evans, M.A., Fahnenstiel, G.L., He, L., Ho, J.C., Jenkins, L., Johengen, T.H., Kuo, K.C., LaPorte, E., Steiner, A.L., Verhamme, E., Wright, D.M., Zagorski, M.A., 2013. Record-setting algal blooms in Lake Erie caused by agricultural and meteorological trends consisten with expected future conditions. Poroc. Natl. Acad. Sci. U.S.A. 110, 6448–6452.
Mikelsons, K., Wang, M., 2018. Interactive online maps make satellite ocean data accessible. Eos Trans. AGU 99. https://doi.org/10.1029/2018EO096563.
Mikelsons, K., Wang, M., 2019. Optimal satellite orbit configuration for global ocean color product coverage. Opt. Express 27, A445–A457.
Mikelsons, K., Wang, M., Jiang, L., 2020. Statistical evaluation of satellite ocean color data retrievals. Remote Sens. Environ. 237, 111601 https://doi.org/10.1016/j.rse.2019.111601.
Miller, W.D., Jr., L.W.H., Adolf, J.E., 2006. Hurricane Isabel generated an unusual fall bloom in Chesapeake Bay. Geophy. Res. Lett. 33, L06612, doi:10.1029/2005GL025658.
Morel, A., Huot, Y., Gentili, B., Werdell, P.J., Hooker, S.B., Franz, B.A., 2007. Examining the consistency of products derived from various ocean color sensors in open ocean (Case 1) waters in the perspective of a multi-sensor approach. Remote Sens. Environ. 111, 69–88.
O'Reilly, J.E., Maritorena, S., Mitchell, B.G., Siegel, D.A., Carder, K.L., Garver, S.A., Kahru, M., McClain, C.R., 1998. Ocean color chlorophyll algorithms for SeaWiFS. J. Geophys. Res. 103, 24937–24953.
O'Reilly, J.E., Werdell, P.J., 2019. Chlorophyll algorithms for ocean color sensors - OC4, OC5 & OC6. Remote Sens. Environ. 229, 32–47.
Ondrusek, M., Lance, V.P., Wang, M., Stengel, E., Kovach, C., Arnone, R., Ladner, S., Goode, W., Gilerson, A., Ahmed, S., El-Habashi, A., Foster, R., Ottaviani, M., Goes, J. I., Gomes, H., McKee, K., Kang, J.W., Hu, C., Cannizzaro, J., Sun, S., English, D., Johnson, B.C., Lee, Z.P., Zoffoli, L., Lin, J., Tufillaro, N., Lalovic, I., Nahorniak, J., Davis, C.O., Twardowski, M., Stockley, N., Voss, K.J., 2017. Report for Dedicated JPSS VIIRS Ocean Color Calibration/Validation Cruise October 2016. In: Lance, V.P. (Ed.), NOAA Technical Report NESDIS 151. NOAA National Environmental Satellite, Data, and Information Service, Silver Spring, Maryland. https://doi.org/10.7289/V5/TR-NESDIS-151.
Ondrusek, M., Lance, V.P., Wang, M., Stengel, E., Kovach, C., Arnone, R., Ladner, S., Goode, W., Gilerson, A., El-Habashi, A., Carrizo, C., Herrera, E., Ahmed, S., Goes, J. I., Gomes, H., McKee, K., Hu, C., Cannizzaro, J., Zhang, Y., Huang, C., English, D., Johnson, B.C., Lee, Z.P., Yu, X., Shang, Z., Tufillaro, N., Lalovic, I., Voss, K.J., 2019. Report for Dedicated JPSS VIIRS Ocean Color Calibration/Validation Cruise May 2018. In: Lance, V.P. (Ed.), NOAA Technical Report NESDIS 152. NOAA National Environmental Satellite, Data, and Information Service, Silver Spring, Maryland. https://doi.org/10.25923/scyb-qf42.
Qi, L., Hu, C., Mikelsons, K., Wang, M., Lance, V., Sun, S., Barnes, B.B., Zhao, J., Zande, D.V., 2020. In search of floating algae and other organisms in global oceans and lakes. Remote Sens. Environ. 239, 111659 https://doi.org/10.1016/j.rse.2020.111659.
Rast, M., Bezy, J.L., Bruzzi, S., 1999. The ESA Medium Resolution Imaging Spectrometer MERIS a review of the instrument and its mission. Int. J. Remote Sens. 20, 1681–1702.
Salomonson, V.V., Barnes, W.L., Maymon, P.W., Montgomery, H.E., Ostrow, H., 1989. MODIS: advanced facility instrument for studies of the Earth as a system. IEEE Trans. Geosci. Remote Sens. 27, 145–153.
Shi, W., Wang, M., 2007. Observations of a Hurricane Katrina-induced phytoplankton bloom in the Gulf of Mexico. Geophy. Res. Lett. 34, L11607. https://doi.org/10.1029/2007GL029724.
Shi, W., Wang, M., 2009a. Green macroalgae blooms in the Yellow Sea during the spring and summer of 2008. J. Geophys. Res. 114, C12010. https://doi.org/10.1029/2009JC005513.
Shi, W., Wang, M., 2009b. Satellite observations of flood-driven Mississippi River plume in the spring of 2008. Geophy. Res. Lett. 36, L07607. https://doi.org/10.1029/2009GL037210.
Shi, W., Wang, M., 2019a. A blended inherent optical property algorithm for global satellite ocean color observations. Limnol. Oceanogr. Methods 17, 377–394.
Shi, W., Wang, M., 2019b. Characterization of suspended particle size distribution in global highly turbid waters from VIIRS measurements. J. Geophys. Res. Oceans 124, 3796–3817.
Shi, W., Wang, M., Li, J., 2020. Water property in high-altitude Qinghai Lake in China. Sci. Remote Sens. 2, 100012 https://doi.org/10.1016/j.srs.2020.100012.
Shi, W., Zhang, Y., Wang, M., 2018. Deriving total suspended matter concentration from the near-infrared-based inherent optical properties over turbid waters: a case study in Lake Taihu. Remote Sens. 10, 333. https://doi.org/10.3390/rs10020333.
Signorini, S.R., Franz, B.A., McClain, C.R., 2015. Chlorophyll variability in the oligotrophic gyres: mechanisms, seasonality and trends. Front. Mar. Sci 2, 1. https://doi.org/10.3389/fmars.2015.00001.
Son, S., Wang, M., 2015. Diffuse attenuation coefficient of the photosynthetically available radiation Kd(PAR) for global open ocean and coastal waters. Remote Sens. Environ. 159, 250–258.
Son, S., Wang, M., 2020. Water quality properties derived from VIIRS measurements in the Great Lakes. Remote Sens. 12, 1605. https://doi.org/10.3390/rs12101605.
Steffen, M.M., Belisle, S., Watson, S.B., Boyer, G.L., Wilhelm, S.W., 2014. Status, causes and controls of cyanobacterial blooms in Lake Erie. J. Great Lakes Res. 40, 215–225.
Stumpf, R.P., 2001. Applications of satellite ocean color sensors for monitoring and predicting harmful algal blooms. Hum. Ecol. Risk Assess 7, 1363–1368.
Stumpf, R.P., Culver, M.E., Tester, P.A., Kirkpatrick, G.J., Pederson, B., Tomlinson, M.C., Truby, E., Ransibrahmanakul, V., Hughes, K., Soracco, M., 2003. Use of satellite imagery and other data for monitoring *Karenia brevis* blooms in the Gulf of Mexico. Harmful Algae 2, 147–160.
Tanaka, K., Okamura, Y., Amano, T., Hiramatsu, M., Shiratama, K., 2009. Development status of the Second-Generation Global Imager (SGLI) on GCOM-C. Proc. SPIE 7474, Sensors, Systems, and Next-Generation Satellites XIII, 74740N, https://doi.org/10.1117/12.830963.
Tomlinson, M.C., Stumpf, R.P., Ransibrahmanakul, V., Truby, E.W., Kirkpatrick, G.J., Pederson, B.A., Vargo, G.A., Heil, C.A., 2004. Evaluation of the use of SeaWiFS imagery for detecting *Karenia Brevis* harmful algal blooms in the eastern Gulf of Mexico. Remote Sens. Environ. 91, 293–303.
Wang, M., 1999. A sensitivity study of SeaWiFS atmospheric correction algorithm: effects of spectral band variations. Remote Sens. Environ. 67, 348–359.
Wang, M., 2007. Remote sensing of the ocean contributions from ultraviolet to near-infrared using the shortwave infrared bands: simulations. Appl. Opt. 46, 1535–1547.
Wang, M., Franz, B.A., 2000. Comparing the ocean color measurements between MOS and SeaWiFS: a vicarious intercalibration approach for MOS. IEEE Trans. Geosci. Remote Sens. 38, 184–197.
Wang, M., Isaacman, A., Franz, B.A., McClain, C.R., 2002. Ocean color optical property data derived from the Japanese Ocean Color and Temperature Scanner and the French Polarization and Directionality of the Earth's Reflectances: a comparison study. Appl. Opt. 41, 974–990.
Wang, M., Jiang, L., 2018. VIIRS-derived ocean color product using the imaging bands. Remote Sens. Environ. 206, 275–286.
Wang, M., Jiang, L., Liu, X., Son, S., Sun, J., Shi, W., Tan, L., Mikelsons, K., Wang, X., Lance, V., 2016. VIIRS ocean color products: a progress update. In: Proc. the IEEE Int. Geosci. Remote Sens. Symposium (IGARSS), 5848–5851, Beijing, China, July 5810–5815, https://doi.org/10.1109/IGARSS.2016.7730528.
Wang, M., Liu, X., Tan, L., Jiang, L., Son, S., Shi, W., Rausch, K., Voss, K., 2013. Impact of VIIRS SDR performance on ocean color products. J. Geophys. Res. Atmos. 118, 10347–10360. https://doi.org/10.1002/jgrd.50793.
Wang, M., Shi, W., 2005. Estimation of ocean contribution at the MODIS near-infrared wavelengths along the east coast of the U.S.: two case studies. Geophys. Res. Lett. 32, L13606. https://doi.org/10.1029/2005GL022917.
Wang, M., Shi, W., 2007. The NIR-SWIR combined atmospheric correction approach for MODIS ocean color data processing. Opt. Express 15, 15722–15733.
Wang, M., Shi, W., Tang, J., 2011. Water property monitoring and assessment for China's inland Lake Taihu from MODIS-Aqua measurements. Remote Sens. Environ. 115, 841–854.
Wang, M., Shi, W., Watanabe, S., 2020. Satellite-measured water properties in high altitude Lake Tahoe. Water Res. 178, 115839 https://doi.org/10.1016/j.watres.2020.115839.
Wang, M., Son, S., 2016. VIIRS-derived chlorophyll-a using the ocean color index method. Remote Sens. Environ. 182, 141–149. https://doi.org/10.1016/j.rse.2016.05.001.
Wang, M., Son, S., L. W. Harding, J., 2009. Retrieval of diffuse attenuation coefficient in the Chesapeake Bay and turbid ocean regions for satellite ocean color applications. J. Geophys. Res. 114, C10011, https://doi.org/10.1029/2009JC005286.
Watson, S.B., Miller, C., Arhonditsis, G., Boyer, G.L., Carmichael, W., Charlton, M.N., Confesor, R., Depew, D.C., Hook, T.O., Ludsin, S.A., Matisoff, G., McElmurry, S.P., Murray, M.W., Richards, R.P., Rao, Y.R., Tteffen, M.M., Wilhelm, S.W., 2016. The re-eutrophication of Lake Erie: Harmful algal blooms and hypoxia. Harmful Algae 56, 44–66.
Wei, J., Lee, Z., Shang, S., 2016. A system to measure the data quality of spectral remote-sensing reflectance of aquatic environments. J. Geophys. Res. Oceans 121, 8189–8207. https://doi.org/10.1002/2016JC012126.
Wei, J., Wang, M., Lee, Z., Briceño, H.O., Yu, X., Jiang, L., Garcia, R., Wang, J., Luis, K., 2020. Shallow water bathymetry with multi-spectral satellite ocean color sensors: leveraging temporal variation in image data. Remote Sens. Environ. 250, 112035 https://doi.org/10.1016/j.rse/2020.112035.
Werdell, P.J., Franz, B.A., Bailey, S.W., Feldman, G.C., Boss, E., Brando, V.E., Dowell, M., Hirata, T., Lavender, S.J., Lee, Z.P., Loisel, H., Maritorena, S., Melin, F., Moore, T.S., Smyth, T.J., Antoine, D., Devred, E., d'Andon, O.H.F., Mangin, A., 2013. Generalized ocean color inversion model for retrieving marine inherent optical properties. Appl. Opt. 52, 2019–2037.
Yu, X., Lee, Z., Shen, F., Wang, M., Wei, J., Jiang, L., Shang, Z., 2019. An empirical algorithm to seamlessly retrieve the concentration of suspended particulate matter from water color across ocean to turbid river mouths. Remote Sens. Environ. 235, 111491 https://doi.org/10.1016/j.rse.2019.111491.